



Article

Measuring Exciton Fine-Structure in Randomly Oriented Perovskite Nanocrystal Ensembles Using Nonlinear Optical Spectroscopy: Theory

Albert Liu

Condensed Matter Dynamics Department, Max Planck Institute for the Structure and Dynamics of Matter, 22761 Hamburg, Germany; albert.liu@mpsd.mpg.de

Abstract: Lead halide perovskite nanocrystals (PNCs) exhibit unique optoelectronic properties, many of which originate from a purported bright-triplet exciton fine-structure. A major impediment to measuring this fine-structure is inhomogeneous spectral broadening, which has limited most experimental studies to single-nanocrystal spectroscopies. It is shown here that the linearly polarized single-particle selection rules in PNCs are preserved in nonlinear spectroscopies of randomly oriented ensembles. Simulations incorporating rotational averaging demonstrate that techniques such as transient absorption and two-dimensional coherent spectroscopy are capable of resolving exciton fine-structure in PNCs, even in the presence of inhomogeneous broadening and orientation disorder.

Keywords: perovskite; nanocrystals; nonlinear spectroscopy; excitons; fine-structure



Citation: Liu, A. Measuring Exciton Fine-Structure in Randomly Oriented Perovskite Nanocrystal Ensembles Using Nonlinear Optical Spectroscopy: Theory. *Nanomaterials* **2022**, *12*, 801. <https://doi.org/10.3390/nano12050801>

Academic Editor: Jiangshan Chen

Received: 7 February 2022

Accepted: 23 February 2022

Published: 26 February 2022

Publisher's Note: MDPI stays neutral with regard to jurisdictional claims in published maps and institutional affiliations.



Copyright: © 2022 by the author. Licensee MDPI, Basel, Switzerland. This article is an open access article distributed under the terms and conditions of the Creative Commons Attribution (CC BY) license (<https://creativecommons.org/licenses/by/4.0/>).

1. Introduction

Semiconductor colloidal nanocrystals, also called colloidal quantum dots, comprise a material platform that has sustained research interest over recent decades due to their numerous potential applications. Indeed, their advantageous optical properties have found use in many areas such as displays [1], photovoltaics [2], and biological tagging [3].

In recent years, successful synthesis of lead halide perovskite nanocrystals (PNCs) [4] has spurred a renaissance in colloidal nanocrystal research. Many properties of PNCs, such as their high defect tolerance [5] and unusual brightness, defy our traditional understanding of colloidal nanocrystals. In particular, recent evidence suggests a bright-triplet exciton ground state as the underlying mechanism for their efficient light emission [6]. Consisting of three nondegenerate states with orthogonal dipole moments [6,7], this bright-triplet state has also exhibited promising quantum-coherent properties such as coherent single-photon emission [8] and superfluorescence [9]. However, the existence of bright-triplet excitons in PNCs is far from conclusive. Indeed, a recent report has argued that the lowest-energy exciton state is in fact a dark singlet state [10], albeit in a perovskite material (FAPbBr₃) different to that of the original report of a bright-triplet exciton ground state (CsPbBr₂Cl) [6]. This controversy both highlights our poor understanding of fine-structure in PNCs and emphasizes the need for new approaches to investigating their underlying physics.

In general, homogeneous properties of colloidal nanocrystals, such as their fine-structure, are difficult to study primarily due to inhomogeneous spectral broadening in ensembles [11,12]. Exciton fine-structure of PNCs have, thus far, primarily been investigated via single-nanocrystal linear fluorescence spectroscopy to circumvent inhomogeneity [13]. This presents two severe limitations. First, fluorescence measurements reveal radiative recombination timescales but are not sensitive to other dynamics such as intraband relaxation and coherence dephasing. Second, single-nanocrystal experiments preclude the measurement of *ensemble-averaged* properties that are relevant for practical applications. Although conventional wisdom from linear techniques suggests that optical spectroscopies only measure the inhomogeneous linewidth of a disordered ensemble, can nonlinear spectroscopies

be used to measure properties of exciton fine-structure in PNCs even in the presence of dominant inhomogeneous broadening? We address this question in the present study.

2. Rotational-Averaging of Optical Responses

In general, spectroscopy via applied electromagnetic fields may be interpreted as measurement of a material's optical response function. In the interest of describing different spectroscopic techniques under a unified framework, we express optical response functions perturbatively (valid in the limit of weak excitation field). For example, induced linear and third-order polarizations may be written:

$$P^{(1)}(t) = \int_{-\infty}^t S^{(1)}(t_1)E(t-t_1)dt_1 \quad (1)$$

$$P^{(3)}(t) = \int_{-\infty}^t \int_{-\infty}^{t_3} \int_{-\infty}^{t_2} S^{(3)}(t_3, t_2, t_1) E(t-t_3)E(t_3-t_2)E(t_2-t_1)dt_1dt_2dt_3 \quad (2)$$

where $S^{(1)}(t_1)$ and $S^{(3)}(t_3, t_2, t_1)$ are the linear and third-order optical response functions, respectively. Here we will assume the impulsive limit (often valid in condensed systems at cryogenic temperatures), in which $P^{(n)}$ becomes identical to $S^{(n)}$ with the appropriate time arguments. Functionally, these optical response functions are constructed from quantum pathways that represent sequences of changes in the system density matrix, where the number of changes corresponds to the perturbative order of a spectroscopy and the probed response function:

$$S^{(n)}(t_n, t_{n-1}, \dots, t_1) = \sum_i \langle C \rangle_i \left[R_i^{(n)}(t_n, t_{n-1}, \dots, t_1) + \text{c.c.} \right] \quad (3)$$

where $\langle C \rangle_i$ are rotational-averaging coefficients [14] which scale each respective quantum pathway $R_i^{(n)}$. The value of $\langle C \rangle_i$ depends on the experimental polarization configuration and the transition selection rules of each quantum pathway, specifically:

$$\langle C \rangle = \sum_{i_1 \dots i_n, \lambda_1 \dots \lambda_n} A_{i_1 \dots i_n} I_{i_1 \dots i_n, \lambda_1 \dots \lambda_n}^{(n)} P_{\lambda_1 \dots \lambda_n} \quad (4)$$

where $A_{i_1 \dots i_n}$ and $P_{\lambda_1 \dots \lambda_n}$ are tensor products of the excitation polarization and transition dipole moment vectors respectively. $I_{i_1 \dots i_n, \lambda_1 \dots \lambda_n}^{(n)}$ is then an interface tensor [15] which rotational-averages the transition strength tensor $P_{\lambda_1 \dots \lambda_n}$ (defined in the nanocrystal reference frame λ_m) according to the polarization tensor $A_{i_1 \dots i_n}$ (defined in the experimental reference frame i_m). Details of the rotational-averaging theory and definitions of $I^{(n)}$ are given in the Supplementary Information. We now apply the above procedure to a concrete system, the bright-triplet fine-structure in PNCs.

3. Fine-Structure in Perovskite Nanocrystals

The relative energies of fine-structure states result from a hierarchy of corrections to the simple spherical quantum well model of nanocrystals. In nanocrystals of inorganic semiconductors, strong electron-hole exchange interaction usually results in a optically-active spin-triplet positioned energetically above a "dark" spin-singlet ground state. In lead halide PNCs, however, the Rashba effect [16] has been shown to play an additional significant role in excitonic fine-structure [7,17] and may result in an optically active bright-triplet ground state [6].

An energy-level diagram of the bright-triplet ground state is shown in Figure 1. The triplet states are denoted $\{|\psi_x\rangle, |\psi_y\rangle, |\psi_z\rangle\}$ according to their dipole moments polarized along the lattice symmetry-axes [6,7]. The orthogonal linear dipole moments of the triplet

states give rise to well-defined optical selection rules, which may be exploited in various spectroscopies of PNCs. The transition dipole moment vectors are then defined:

$$\boldsymbol{\mu}_X = \begin{pmatrix} 1 \\ 0 \\ 0 \end{pmatrix}, \quad \boldsymbol{\mu}_Y = \begin{pmatrix} 0 \\ 1 \\ 0 \end{pmatrix}, \quad \boldsymbol{\mu}_Z = \begin{pmatrix} 0 \\ 0 \\ 1 \end{pmatrix} \quad (5)$$

which, to emphasize, are defined in the nanocrystal reference frame. It was previously shown by Scholes [14] that circularly polarized selection rules are preserved in a rotational-averaged nanocrystal ensemble, which is not entirely surprising when considering the decomposition of a circularly polarized basis into two (orthogonal) out-of-phase linearly polarized components that span the experimental observation plane. However, it is less obvious whether the linearly polarized selection rules of PNCs persist upon rotational-averaging.

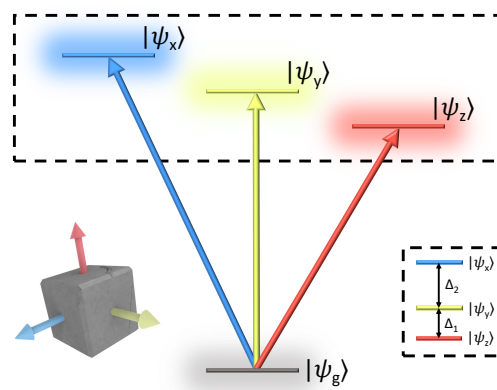


Figure 1. Fine-structure of orthorhombic phase perovskite nanocrystals. Transitions from the excitonic ground state $|\psi_g\rangle$ to the bright triplet states $|\psi_i\rangle$, where $i = \{x, y, z\}$, are polarized along the orthorhombic symmetry axes. We note that the case of a fully nondegenerate triplet manifold shown here assumes an orthorhombic phase perovskite lattice [10].

4. Four-Wave Mixing

In generic terms, four-wave mixing (FWM) describes sets of four field-matter interactions mediated by the third-order optical response of a material. For example, two-photon absorption is a FWM process involving four field-excitation interactions from a single applied field, and is thus proportional to the excitation intensity squared. In the most general case shown in Figure 2a however, each field-matter interaction may arise from a distinct applied field, in which three excitation pulses $\{A, B, C\}$ generate an emitted FWM signal E_{FWM} via the third-order optical response function $S^{(3)}$.

The higher dimensionality of $S^{(3)}$ affords correspondingly more numerous experimental degrees of freedom. For measurement of fine-structure in PNCs in particular, varying the polarizations of each excitation pulse yields access to a much richer set of phenomena *between* triplet states. We examine three polarization configurations shown in Figure 2b, which we denote colinear, cross-linear pump-probe (cross-PP), and cross-linear transient-grating (cross-TG). The rotational averaging coefficients for each polarization scheme are listed in Table 1. We note that excitation with cross-PP and cross-TG result in a negative coefficient (C) (resulting in a half-period phase shift of the emitted signal) for certain dipole transition sequences, which has also been predicted and observed for circularly-polarized selection rules [14,18]. To answer whether the triplet-exciton selection rules persist in a randomly oriented ensemble, we first simulate, for each polarization configuration, the total rotational-averaged FWM signal from the energy level structure plotted in Figure 1 with energy splittings $\Delta_1 = 0.8$ meV and $\Delta_2 = 2.2$ meV. Dephasing and population relaxation times of $T_2 = 25$ ps and $T_1 = 200$ ps respectively are assumed for all three triplet state

transitions [19], and completely orthogonal dipole moments for the three triplet states (not the case in real PNCs [6,10,20]) are assumed for simplicity. Finally, a Gaussian distribution of the fundamental exciton resonance energy is introduced (of $\sigma = 40$ meV) to mimic the inhomogeneous size distribution of the ensemble. As shown in Figure 2c the FWM signal indeed remains polarized and varies with excitation polarization, demonstrating the feasibility of polarization-resolved FWM measurements to probe triplet-state fine-structure in PNC ensembles.

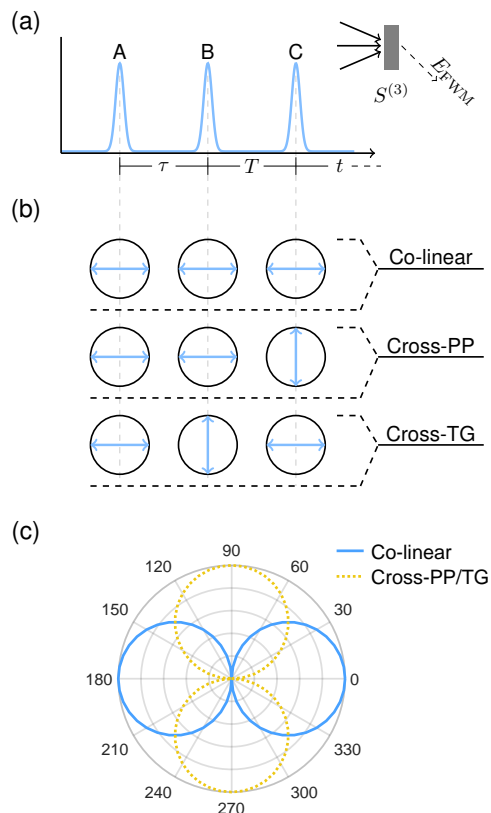


Figure 2. (a) General FWM pulse-ordering diagram. (b) Schematics of colinear, cross-linear pump-probe (cross-PP), and cross-linear transient-grating (cross-TG) polarization schemes. Indicated polarizations correspond to pulses A, B, and C from left to right respectively. (c) Calculated polarization dependences of the rotational-averaged FWM signals for each polarization scheme, in which the linearly-polarized selection rules are preserved.

Table 1. Rotational-averaging coefficients $\langle C \rangle$ of third-order quantum pathways beginning with excitation of $|\psi_x\rangle$ for each polarization scheme. Remaining coefficients may be determined by cyclic permutation of the dipole moments $\{\mu_x, \mu_y, \mu_z\}$.

$A_{i_1 i_2 i_3 i_4}$	$P_{\lambda_1 \lambda_2 \lambda_3 \lambda_4}$	$\langle C \rangle$
$P_x \otimes P_x \otimes P_x \otimes P_x$	$\mu_x \otimes \mu_x \otimes \mu_x \otimes \mu_x$	$\frac{1}{5}$
$P_x \otimes P_x \otimes P_x \otimes P_x$	$\mu_x \otimes \mu_y \otimes \mu_x \otimes \mu_y$	$\frac{1}{15}$
$P_x \otimes P_x \otimes P_x \otimes P_x$	$\mu_x \otimes \mu_z \otimes \mu_x \otimes \mu_z$	$\frac{1}{15}$
$P_x \otimes P_x \otimes P_x \otimes P_x$	$\mu_x \otimes \mu_x \otimes \mu_y \otimes \mu_y$	$\frac{1}{15}$
$P_x \otimes P_x \otimes P_x \otimes P_x$	$\mu_x \otimes \mu_x \otimes \mu_z \otimes \mu_z$	$\frac{1}{15}$
$P_x \otimes P_x \otimes P_y \otimes P_y$	$\mu_x \otimes \mu_x \otimes \mu_x \otimes \mu_x$	$\frac{1}{15}$
$P_x \otimes P_x \otimes P_y \otimes P_y$	$\mu_x \otimes \mu_y \otimes \mu_x \otimes \mu_y$	$-\frac{1}{30}$
$P_x \otimes P_x \otimes P_y \otimes P_y$	$\mu_x \otimes \mu_z \otimes \mu_x \otimes \mu_z$	$-\frac{1}{30}$
$P_x \otimes P_x \otimes P_y \otimes P_y$	$\mu_x \otimes \mu_x \otimes \mu_y \otimes \mu_y$	$\frac{2}{15}$
$P_x \otimes P_x \otimes P_y \otimes P_y$	$\mu_x \otimes \mu_x \otimes \mu_z \otimes \mu_z$	$\frac{2}{15}$

Table 1. Cont.

$A_{i_1 i_2 i_3 i_4}$	$P_{\lambda_1 \lambda_2 \lambda_3 \lambda_4}$	$\langle C \rangle$
$\mathbf{p}_X \otimes \mathbf{p}_Y \otimes \mathbf{p}_X \otimes \mathbf{p}_Y$	$\mu_X \otimes \mu_X \otimes \mu_X \otimes \mu_X$	$\frac{1}{15}$
$\mathbf{p}_X \otimes \mathbf{p}_Y \otimes \mathbf{p}_X \otimes \mathbf{p}_Y$	$\mu_X \otimes \mu_Y \otimes \mu_X \otimes \mu_Y$	$\frac{2}{15}$
$\mathbf{p}_X \otimes \mathbf{p}_Y \otimes \mathbf{p}_X \otimes \mathbf{p}_Y$	$\mu_X \otimes \mu_Z \otimes \mu_X \otimes \mu_Z$	$\frac{2}{15}$
$\mathbf{p}_X \otimes \mathbf{p}_Y \otimes \mathbf{p}_X \otimes \mathbf{p}_Y$	$\mu_X \otimes \mu_X \otimes \mu_Y \otimes \mu_Y$	$-\frac{1}{30}$
$\mathbf{p}_X \otimes \mathbf{p}_Y \otimes \mathbf{p}_X \otimes \mathbf{p}_Y$	$\mu_X \otimes \mu_X \otimes \mu_Z \otimes \mu_Z$	$-\frac{1}{30}$

Transient Absorption (Pump-Probe)

Transient absorption spectroscopy is a spectroscopic technique commonly used to measure excited state dynamics in colloidal nanocrystals. Specifically, an initial (pump) pulse excites a material into a nonequilibrium state and the pump-induced (often spectrally resolved) change in absorption of a subsequent (probe) pulse is measured. By performing these measurements as a function of the inter-pulse time-delay, dynamics such as intraband energy redistribution and interband relaxation may be resolved on ultrafast timescales.

Transient absorption spectroscopy may also be framed in a more general four-wave mixing perspective. For the pulse sequence in Figure 2a, we may set $\tau = 0$ so that pulses *A* and *B* are jointly equivalent to the initial pump pulse and pulse *C* acts as the probe pulse. Assuming an infinitely broad probe pulse spectrum (which approximates the usual case of a white-light continuum probe pulse), the real-quadrature of the resultant optical response function then provides the transient absorption signal [21,22]:

$$\Delta A(\omega_t, T) \approx \text{Re} \int_{-\infty}^{\infty} E_{\text{pump}}(\omega_\tau) S^{(3)}(\omega_t, T, \omega_\tau) d\omega_\tau \quad (6)$$

where the response function $S^{(3)}(\omega_t, T, \omega_\tau)$ has been Fourier transformed along the variables τ and t into frequency-space. The pump-spectrum $E_{\text{pump}}(\omega)$ then windows the optical response, enabling varying degrees of spectral selectivity.

We now simulate transient absorption spectra of PNCs by enumerating all quantum pathways comprising the third-order optical response. There are three categories of third-order quantum pathways $R^{(3)}$, named excited-state emission (ESE), ground-state bleach (GSB), and excited-state absorption (ESA), each of which corresponds to a distinct dynamical process. In order, ESE is a negative change in absorption arising from a pump-induced excited-state population which then undergoes emission stimulated by the probe pulse. GSB is also a negative absorption change due to pump-induced depletion of the absorption ground state. ESA is the only positive absorption change from a singly to doubly excited (biexciton) state transition, which is neglected here. The third-order response function may be calculated by summing each ESE, GSB, and ESA quantum pathway (detailed in the Supplemental Information), and the resultant rotational-averaged transient absorption spectra are plotted in Figure 3. For broadband excitation (FWHM = 1 and 2 meV), a broad absorption bleach feature appears at $E - E_{\text{pump}} = 0$ from the band-edge exciton transitions. Upon narrowing the excitation bandwidth (FWHM = 0.2 meV), narrow features that arise from absorption and emission involving different pairs of triplet states appear. The energy of each peak then corresponds to the energy separation of the two triplet states involved.

Although transient absorption measurements with narrowband excitation can characterize triplet state energy splittings of a PNC ensemble, this method has certain drawbacks. For example, the linewidths of the fine-structure features are convolved with the pump spectral width, which interferes with extracting the homogeneous linewidth of each transition. The primary disadvantage arises from the time-bandwidth product relation for transform-limited pulses, which informs a minimum pulse duration for a given spectral bandwidth. For example, a spectral bandwidth of 0.2 meV centered at 2590 meV requires a pulse duration greater than approximately 3 picoseconds (far longer than the femtosecond pulses typically used to measure ultrafast processes in both molecular and condensed systems [23]). Indeed, one may consider narrow pump-bandwidth transient absorption

measurements as approaching the limit of continuous-wave spectral hole burning [24]. Ultrafast dynamical processes of the triplet-state manifold, such as spectral diffusion or energy transfer, thus require a more advanced spectroscopic technique to resolve.

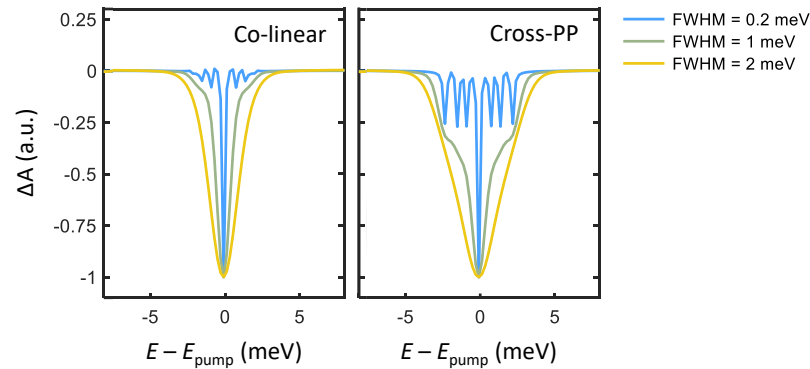


Figure 3. Transient absorption simulated for co-linear (**left**) and cross-linear (**right**) excitation at a pump-probe delay $T = 1$ ps. Three curves of varying pump spectral selectivity are simulated for each polarization scheme, with pump spectra centered at $E_{\text{pump}} = 2590$ meV and FWHM of 0.2, 1, and 2 meV.

5. Two-Dimensional Coherent Spectroscopy

Two-dimensional coherent spectroscopy (2DCS), or more generally multidimensional coherent spectroscopy [25–27], is a nonlinear spectroscopic technique capable of resolving all dimensions of a complex-valued nonlinear optical response. As the name implies, a 2-D spectrum is obtained that reflects a cross section of $S^{(n)}$ along two spectral axes. In doing so, it offers many advantages over other one-dimensional spectroscopies that probe only an integrated cross section of $S^{(n)}$ (such as the previously discussed transient absorption spectroscopy).

To perform 2DCS of a third-order optical response, a transient FWM signal is measured as a function of two time variables (see Figure 2a). As described above, this corresponds to direct measurement of $S^{(3)}(t, T, \tau)$ in the impulsive limit. By Fourier transforming $S^{(3)}$ along the two time axes, a 2-D spectrum is produced that correlates the dynamics of a system following each excitation pulse. As a Fourier transform spectroscopy, the spectral resolution of 2DCS is determined by the maximum measurement time delays (irrespective of excitation spectral bandwidth) and is therefore ideal for measuring low-energy excitations. For example, achieving an energy resolution of 0.8 meV, corresponding to the smallest energy splitting Δ_1 considered here, requires a maximum time delay of approximately 5 ps. Here, we discuss two types of third-order 2-D spectra relevant to measuring fine-structure in PNCs, namely one-quantum and zero-quantum 2-D spectra.

5.1. One-Quantum 2-D Spectra

Rephasing one-quantum spectra are obtained by Fourier transforming a photon echo FWM signal [28] along the time variables τ and t , which correlates the absorption and emission dynamics of a material (along the two conjugate axes ω_τ and ω_t , respectively) in $S(\omega_t, T, \omega_\tau)$. The rephasing nature of the photon echo FWM signal, reflected in the oppositely signed frequencies ω_τ and ω_t , separates homogeneous and inhomogeneous broadening contributions to resonance linewidths in two-dimensional frequency space [29,30], and is therefore ideal in studying disordered materials such as nanocrystal ensembles [12,31]. Though the full complex-valued spectrum contains unique information concerning many-body effects in a given system [32–34], we present only absolute value spectra here for simplicity. One-quantum spectra of perovskite nanocrystals, simulated for the three excitation polarization schemes defined in Figure 2, are shown in Figure 4. A single primary feature is evident in the colinear excitation spectrum, namely a peak along the diagonal line ($|\hbar\omega_\tau| = |\hbar\omega_t|$) arising from resonant absorption and emission involving

the bright-triplet exciton states. With cross-PP and cross-TG excitation, sidebands around the diagonal peak appear to correspond to sequential absorption and emission involving different triplet states. We note that infinite excitation laser bandwidth is assumed in these simulations, in which the extent of the peaks along the diagonal direction reflect the inhomogeneous distribution of the fundamental exciton resonance energy ($\sigma = 40$ meV). In the case of finite excitation bandwidth on the scale of the resonance energy distribution, the 2-D spectrum is windowed accordingly (which may cause lineshape distortions towards the edges) [31].

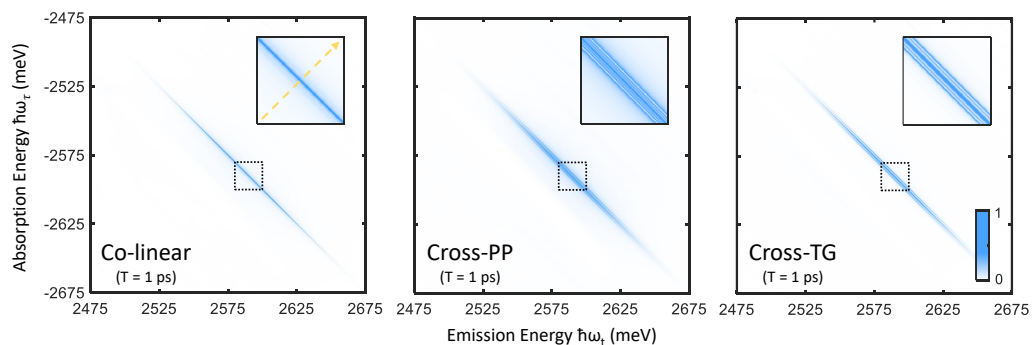


Figure 4. Rephasing one-quantum spectra simulated for colinear (left), cross-PP (middle), and cross-TG (right) excitation and $T = 1$ ps. The sections of the spectra outlined by the dashed boxes are plotted inset, which show the appearance of sidebands with cross-PP and cross-TG excitation. The yellow dashed arrow in the left inset plot indicates the position and direction of the cross-diagonal slices shown in Figure 5.

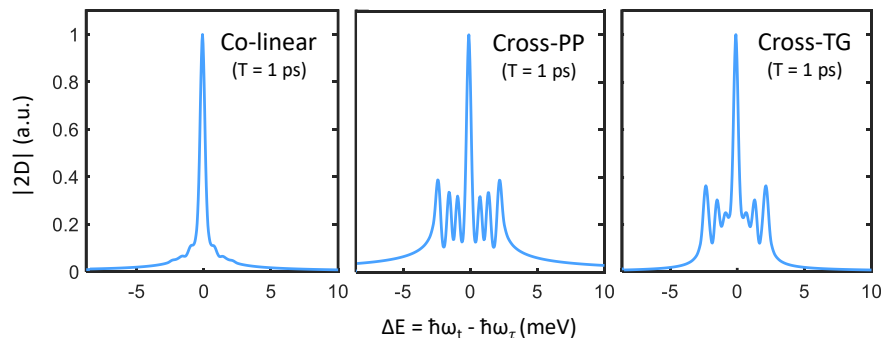


Figure 5. Cross-diagonal slices centered at $|\hbar\omega_t| = |\hbar\omega_\tau| = 2590$ meV from the three one-quantum spectra plotted in Figure 4. Signatures of the triplet-state fine-structure manifest in the cross-PP and cross-TG slices, while being suppressed in the colinear slice.

We can examine these features more closely by taking slices along the direction perpendicular to the diagonal line (indicated by the dashed yellow arrow in Figure 4). Cross-diagonal slices centered at $|\hbar\omega_t| = |\hbar\omega_\tau| = 2590$ meV are plotted in Figure 5, which make obvious the analogy to transient absorption spectra. Just as in the narrow-excitation bandwidth transient absorption spectra in Figure 3, coherent coupling peaks appearing at $\Delta E = \{\pm\Delta_1, \pm\Delta_2, \pm(\Delta_1 + \Delta_2)\}$ become prominent with cross-PP and cross-TG excitation. Although from summing the allowed quantum pathways, one would expect identical peak amplitudes between cross-PP and cross-TG excitation, this is not observed in Figure 5. The reason for this discrepancy is the difference in rotational-averaging coefficients as shown in Table 1, which favor quantum pathways involving intermediate population states (that exhibit monotonic population relaxation during T) with cross-PP excitation and intermediate intraband coherences (that exhibit phase evolution during T) with cross-TG excitation. While the chosen value of $T = 1$ ps is arbitrary, changing the intermediate time-delay T results in variation of the relative phases of each sideband as well as their sub-

sequent interference lineshapes. These simulations thus show that rephasing one-quantum spectra can resolve both energy splittings and homogeneous lineshapes of the exciton fine-structure in perovskite nanocrystals.

5.2. Zero-Quantum 2-D Spectra

In addition to measuring interband coherences arising from superpositions of ground and excited exciton states, 2DCS is also capable of resolving the dynamics of intraband coherences due to superpositions of two nondegenerate exciton states split by an energy within the excitation laser bandwidth. This is done by measurement of zero-quantum spectra [35,36], which are usually obtained by Fourier transforming a photon echo FWM signal along the time variables T and t , which correlate the emission dynamics of a material with intermediate population relaxation or intraband coherence oscillations (along the two conjugate axes ω_t and ω_T respectively) in $S(\omega_t, \omega_T, \tau)$.

Zero-quantum spectra of perovskite nanocrystals are shown in Figure 6, in which primary peaks at $\hbar\omega_T = 0$ as well as sidebands at finite mixing frequency are observed. The strong central peaks may be attributed to nonoscillatory population relaxation dynamics, while the sidebands correspond to intraband coherence oscillations between pairs of bright triplet states (we note that triplet states involved in the probed intraband coherences need not be directly coupled by transition dipoles [35], and simply require a shared common ground state). Vertical slices taken along $\hbar\omega_t = 2590$ meV are also shown in Figure 6, which shows that the intraband coherence response is enhanced by cross-PP and cross-TG excitation while being suppressed by colinear excitation. The linewidths of the central peaks and sidebands then inform the average population relaxation rate and intraband coherence dephasing rates respectively [20].

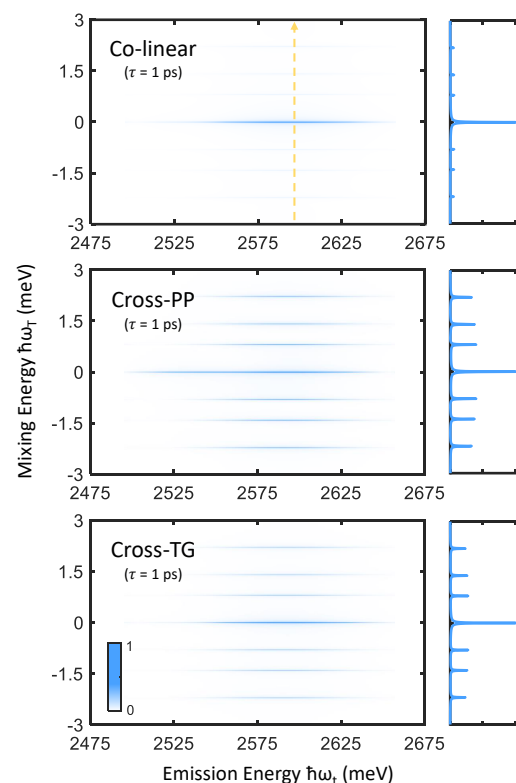


Figure 6. Zero-quantum spectra simulated for colinear (**top**), cross-PP (**middle**), and cross-TG (**bottom**) excitation and $\tau = 1$ ps. Vertical slices taken along $\hbar\omega_t = 2590$ meV (indicated by the dashed yellow arrow) are plotted to the right of each spectrum, which emphasize the effect of excitation polarization scheme on the intraband coherence response.

5.3. Other Structural Phases

The fully nondegenerate triplet fine-structure considered thus far assumes an orthorhombic phase perovskite lattice [10]. However, lead halide perovskites are known to exhibit successive structural phase transitions into tetragonal and cubic crystal phases with increasing temperature [37]. The increasing symmetry of the tetragonal and cubic phases reduces the triplet fine-structure to two and one nondegenerate level(s) respectively, which naturally lead to changes in both their linear and nonlinear spectra.

In the current context, the nonlinear optical responses of tetragonal and cubic phase crystals may be interpreted and calculated in an identical manner for orthorhombic phase perovskites (as described here). With fewer energy splittings in the fine-structure, the transient absorption and 2-D spectra mainly differ in the number of resultant sidebands, from six sidebands in the orthorhombic phase to two sidebands and zero sidebands in the tetragonal and cubic phases respectively.

6. Conclusions

We have presented the general framework for rotational-averaging a perturbative optical response, with applications to spectroscopy of randomly oriented ensembles of PNCs. Via simulations of transient absorption and 2DCS spectra, we showed that the linearly polarized single-particle selection rules of PNCs manifest in nonlinear spectroscopies of PNC ensembles with appropriate excitation polarization schemes. In particular, one-quantum and zero-quantum spectra can characterize the energy splittings and homogeneous lineshapes of the triplet state fine-structure even in the presence of both inhomogeneous broadening and orientation disorder, which has been confirmed in a recent experimental study [20].

We emphasize that the applications of nonlinear spectroscopy to PNC ensembles extend beyond resolving the bright-triplet exciton fine-structure, the focus of the present work. For example, the directional dipole-moments of vibrational modes in lead halide perovskites may translate to anisotropic exciton-phonon coupling, which would also manifest in a rotational-averaged optical response. Following recent work on magneto-PL spectroscopy of PNCs [10], magnetic-field brightening of the singlet dark state [13] may be similarly exploited in nonlinear spectroscopy of PNCs. In particular, coupling features between bright and dark states in 2DCS spectra will inherit both the polarization selection rules of the triplet states and their strong oscillator strength [38], and therefore serve as a direct probe of the fundamental optical properties of the dark state. Simultaneously resolving the homogeneous lineshapes of dark-singlet and bright-triplet states will inform the coupling mechanisms between them, and more generally the microscopic origin of exciton fine-structure in PNCs.

Supplementary Materials: The following supporting information can be downloaded at: <https://www.mdpi.com/article/10.3390/nano12050801/s1>. Enumerating Quantum Pathways Using Feynman Diagrams; Analytical Form of the Optical Response Functions; Theory of Rotational-Averaging.

Funding: The APC was funded by the Max Planck Digital Library. Albert Liu was supported by a fellowship from the Alexander von Humboldt Foundation.

Data Availability Statement: Not applicable.

Conflicts of Interest: The authors declare no conflict of interest. The funders had no role in the design of the study; in the collection, analyses, or interpretation of data; in the writing of the manuscript, or in the decision to publish the results.

References

1. Choi, M.K.; Yang, J.; Hyeon, T.; Kim, D.H. Flexible quantum dot light-emitting diodes for next-generation displays. *NPJ Flex. Electron.* **2018**, *2*, 10. [[CrossRef](#)]
2. Carey, G.H.; Abdelhady, A.L.; Ning, Z.; Thon, S.M.; Bakr, O.M.; Sargent, E.H. Colloidal Quantum Dot Solar Cells. *Chem. Rev.* **2015**, *115*, 12732–12763. [[CrossRef](#)]

3. Martynenko, I.V.; Litvin, A.P.; Purcell-Milton, F.; Baranov, A.V.; Fedorov, A.V.; Gun'ko, Y.K. Application of semiconductor quantum dots in bioimaging and biosensing. *J. Mater. Chem. B* **2017**, *5*, 6701–6727. [[CrossRef](#)] [[PubMed](#)]
4. Protesescu, L.; Yakunin, S.; Bodnarchuk, M.I.; Krieg, F.; Caputo, R.; Hendon, C.H.; Yang, R.X.; Walsh, A.; Kovalenko, M.V. Nanocrystals of Cesium Lead Halide Perovskites (CsPbX₃, X = Cl, Br, and I): Novel Optoelectronic Materials Showing Bright Emission with Wide Color Gamut. *Nano Lett.* **2015**, *15*, 3692–3696. [[CrossRef](#)] [[PubMed](#)]
5. Huang, H.; Bodnarchuk, M.I.; Kershaw, S.V.; Kovalenko, M.V.; Rogach, A.L. Lead Halide Perovskite Nanocrystals in the Research Spotlight: Stability and Defect Tolerance. *ACS Energy Lett.* **2017**, *2*, 2071–2083. [[CrossRef](#)] [[PubMed](#)]
6. Becker, M.A.; Vaxenburg, R.; Nedelcu, G.; Sercel, P.C.; Shabaev, A.; Mehl, M.J.; Michopoulos, J.G.; Lambrakos, S.G.; Bernstein, N.; Lyons, J.L.; et al. Bright triplet excitons in caesium lead halide perovskites. *Nature* **2018**, *553*, 189–193. [[CrossRef](#)]
7. Sercel, P.C.; Lyons, J.L.; Wickramaratne, D.; Vaxenburg, R.; Bernstein, N.; Efros, A.L. Exciton Fine Structure in Perovskite Nanocrystals. *Nano Lett.* **2019**, *19*, 4068–4077. [[CrossRef](#)]
8. Utzat, H.; Sun, W.; Kaplan, A.E.K.; Krieg, F.; Ginterseder, M.; Spokoyny, B.; Klein, N.D.; Shulenberger, K.E.; Perkinson, C.F.; Kovalenko, M.V.; et al. Coherent single-photon emission from colloidal lead halide perovskite quantum dots. *Science* **2019**, *363*, 1068. [[CrossRef](#)]
9. Rainò, G.; Becker, M.A.; Bodnarchuk, M.I.; Mahrt, R.F.; Kovalenko, M.V.; Stöferle, T. Superfluorescence from lead halide perovskite quantum dot superlattices. *Nature* **2018**, *563*, 671–675. [[CrossRef](#)]
10. Tamarat, P.; Bodnarchuk, M.I.; Trebbia, J.B.; Erni, R.; Kovalenko, M.V.; Even, J.; Lounis, B. The ground exciton state of formamidinium lead bromide perovskite nanocrystals is a singlet dark state. *Nat. Mater.* **2019**, *18*, 717–724. [[CrossRef](#)]
11. Liu, A.; Bonato, L.G.; Sessa, F.; Almeida, D.B.; Isele, E.; Nagamine, G.; Zagonel, L.F.; Nogueira, A.F.; Padilha, L.A.; Cundiff, S.T. Effect of dimensionality on the optical absorption properties of CsPbI₃ perovskite nanocrystals. *J. Chem. Phys.* **2019**, *151*, 191103. [[CrossRef](#)]
12. Liu, A.; Nagamine, G.; Bonato, L.G.; Almeida, D.B.; Zagonel, L.F.; Nogueira, A.F.; Padilha, L.A.; Cundiff, S.T. Toward Engineering Intrinsic Line Widths and Line Broadening in Perovskite Nanoplatelets. *ACS Nano* **2021**, *15*, 6499–6506. [[CrossRef](#)] [[PubMed](#)]
13. Fernée, M.J.; Tamarat, P.; Lounis, B. Spectroscopy of single nanocrystals. *Chem. Soc. Rev.* **2014**, *43*, 1311–1337. [[CrossRef](#)] [[PubMed](#)]
14. Scholes, G.D. Selection rules for probing biexcitons and electron spin transitions in isotropic quantum dot ensembles. *J. Chem. Phys.* **2004**, *121*, 10104–10110. [[CrossRef](#)] [[PubMed](#)]
15. Andrews, D.L.; Thirunamachandran, T. On three-dimensional rotational averages. *J. Chem. Phys.* **1977**, *67*, 5026–5033. [[CrossRef](#)]
16. Rashba, E.I.; Sherman, E.Y. Spin-orbital band splitting in symmetric quantum wells. *Phys. Lett. A* **1988**, *129*, 175–179. [[CrossRef](#)]
17. Isarov, M.; Tan, L.Z.; Bodnarchuk, M.I.; Kovalenko, M.V.; Rappe, A.M.; Lifshitz, E. Rashba Effect in a Single Colloidal CsPbBr₃ Perovskite Nanocrystal Detected by Magneto-Optical Measurements. *Nano Lett.* **2017**, *17*, 5020–5026. [[CrossRef](#)]
18. Scholes, G.D.; Kim, J.; Wong, C.Y. Exciton spin relaxation in quantum dots measured using ultrafast transient polarization grating spectroscopy. *Phys. Rev. B* **2006**, *73*, 195325. [[CrossRef](#)]
19. Becker, M.A.; Scarpelli, L.; Nedelcu, G.; Rainò, G.; Masia, F.; Borri, P.; Stöferle, T.; Kovalenko, M.V.; Langbein, W.; Mahrt, R.F. Long Exciton Dephasing Time and Coherent Phonon Coupling in CsPbBr₂Cl Perovskite Nanocrystals. *Nano Lett.* **2018**, *18*, 7546–7551. [[CrossRef](#)]
20. Liu, A.; Almeida, D.B.; Bonato, L.G.; Nagamine, G.; Zagonel, L.F.; Nogueira, A.F.; Padilha, L.A.; Cundiff, S.T. Multidimensional coherent spectroscopy reveals triplet state coherences in cesium lead-halide perovskite nanocrystals. *Sci. Adv.* **2021**, *7*, eabb3594. [[CrossRef](#)]
21. Do, T.N.; Gelin, M.F.; Tan, H.S. Simplified expressions that incorporate finite pulse effects into coherent two-dimensional optical spectra. *J. Chem. Phys.* **2017**, *147*, 144103. [[CrossRef](#)] [[PubMed](#)]
22. Kramer, T.; Rodríguez, M.; Zelinskyy, Y. Modeling of Transient Absorption Spectra in Exciton—Charge-Transfer Systems. *J. Phys. Chem. B* **2017**, *121*, 463–470. [[CrossRef](#)]
23. Berera, R.; van Grondelle, R.; Kennis, J.T.M. Ultrafast transient absorption spectroscopy: Principles and application to photosynthetic systems. *Photosynth. Res.* **2009**, *101*, 105–118. [[CrossRef](#)] [[PubMed](#)]
24. Liu, A.; Cundiff, S.T. Spectroscopic signatures of electron-phonon coupling in silicon-vacancy centers in diamond. *Phys. Rev. Mater.* **2020**, *4*, 055202. [[CrossRef](#)]
25. Cundiff, S.T.; Mukamel, S. Optical multidimensional coherent spectroscopy. *Phys. Today* **2013**, *66*, 44–49. [[CrossRef](#)]
26. Smallwood, C.L.; Cundiff, S.T. Multidimensional Coherent Spectroscopy of Semiconductors. *Laser Photonics Rev.* **2018**, *12*, 1800171. [[CrossRef](#)]
27. Liu, A.; Almeida, D.B.; Padilha, L.A.; Cundiff, S.T. Perspective: Multi-dimensional coherent spectroscopy of perovskite nanocrystals. *J. Phys. Mater.* **2022**, *5*, 021002. [[CrossRef](#)]
28. Cundiff, S.T. Optical Techniques for Solid-State Materials Characterization. In *Optical Techniques for Solid-State Materials Characterization*; Prasankumar, R.P., Taylor, A.J., Eds.; CRC Press: Boca Raton, FL, USA, 2012; Chapter 10, pp. 373–399.
29. Siemens, M.E.; Moody, G.; Li, H.; Bristow, A.D.; Cundiff, S.T. Resonance lineshapes in two-dimensional Fourier transform spectroscopy. *Opt. Express* **2010**, *18*, 17699–17708. [[CrossRef](#)]
30. Liu, A.; Cundiff, S.T.; Almeida, D.B.; Ulbricht, R. Spectral broadening and ultrafast dynamics of a nitrogen-vacancy center ensemble in diamond. *Mater. Quantum. Technol.* **2021**, *1*, 025002. [[CrossRef](#)]

31. Liu, A.; Almeida, D.B.; Bae, W.K.; Padilha, L.A.; Cundiff, S.T. Simultaneous Existence of Confined and Delocalized Vibrational Modes in Colloidal Quantum Dots. *J. Phys. Chem. Lett.* **2019**, *10*, 6144–6150. [[CrossRef](#)]
32. Li, X.; Zhang, T.; Borca, C.N.; Cundiff, S.T. Many-Body Interactions in Semiconductors Probed by Optical Two-Dimensional Fourier Transform Spectroscopy. *Phys. Rev. Lett.* **2006**, *96*, 057406. [[CrossRef](#)] [[PubMed](#)]
33. Kasprzak, J.; Patton, B.; Savona, V.; Langbein, W. Coherent coupling between distant excitons revealed by two-dimensional nonlinear hyperspectral imaging. *Nat. Photonics* **2011**, *5*, 57–63. [[CrossRef](#)]
34. Martin, E.W.; Cundiff, S.T. Inducing coherent quantum dot interactions. *Phys. Rev. B* **2018**, *97*, 081301. [[CrossRef](#)]
35. Yang, L.; Zhang, T.; Bristow, A.D.; Cundiff, S.T.; Mukamel, S. Isolating excitonic Raman coherence in semiconductors using two-dimensional correlation spectroscopy. *J. Chem. Phys.* **2008**, *129*, 234711. [[CrossRef](#)]
36. Liu, A.; Almeida, D.B.; Bae, W.K.; Padilha, L.A.; Cundiff, S.T. Non-Markovian Exciton-Phonon Interactions in Core-Shell Colloidal Quantum Dots at Femtosecond Timescales. *Phys. Rev. Lett.* **2019**, *123*, 057403. [[CrossRef](#)]
37. Chen, C.; Hu, X.; Lu, W.; Chang, S.; Shi, L.; Li, L.; Zhong, H.; Han, J.B. Elucidating the phase transitions and temperature-dependent photoluminescence of MAPbBr₃ single crystal. *J. Phys. D Appl. Phys.* **2018**, *51*, 045105. [[CrossRef](#)]
38. Tollerud, J.O.; Cundiff, S.T.; Davis, J.A. Revealing and Characterizing Dark Excitons through Coherent Multidimensional Spectroscopy. *Phys. Rev. Lett.* **2016**, *117*, 097401. [[CrossRef](#)]